Proceedings of the ASME 2010 3rd Joint US-European Fluids Engineering Summer Meeting and 8th International Conference on Nanochannels, Microchannels, and Minichannels
FEDSM-ICNMM2010
August 1-5, 2010, Montreal, Canada

FEDSM-ICNMM2010-30375

Combined Experimental/Numerical Development of Propulsor Evaluation Capability

Amanda M. Dropkin, Dr. Stephen A. Huyer, and Dr. Charles Henoch
Naval Undersea Warfare Center
Code 8233, Bldg. 1302/2
Newport, RI 02841
Amanda.Dropkin@navy.mil

ABSTRACT

Propulsor design methods utilize Computational Fluid Dynamics (CFD) to develop initial propulsor configurations and predict the full-scale in-water performance of these optimal designs. However, like all numerical models, these CFD models need experimental validation to provide a sufficient level of confidence in the design. The actual data needed to validate CFD models include propulsor inflow velocities and thrust and are impractical to collect for full-scale vehicles. As a result, the in-water propulsor performance can be significantly different than CFD predictions. Another approach in the propulsor design process is to experimentally test a subscale version of the vehicle and appropriately scale results. This scaling is often unreliable due to differences between open water conditions and the flow in the laboratory facility. This paper presents a method to combine CFD modeling with subscale experiments to improve full-scale propulsor performance prediction. Laboratory experiments were conducted on subscale generic torpedo models in the 12'' x 12" water tunnel located at the Naval Undersea Warfare Center in Newport, Rhode Island. This model included an operational ducted post-swirl propulsor. Laser Doppler Velocimetry was used to measure several velocity profiles along the torpedo hull. The experimental data were used in this project to validate the CFD models constructed using the commercial CFD software, Fluent®. Initially, axisymmetric two-dimensional simulations investigated the bare body, hull only case, and a shrouded body without the propulsor. These models were selected to understand the axisymmetric flow development and investigate methods to best match the propulsor inflow. A variety of turbulence models including the realizable k-epsilon model and the Spallart-Almaras model were investigated and ultimately the numerical and experimental velocity profiles were found to match within 3%. Based on these water tunnel simulations, differences between the flow in the facility and open water could then be characterized. These differences quantified both the effect of Reynolds number as well as local flow acceleration due to tunnel blockage effects. Full 3-D flow simulations were then conducted with an operating propulsor and compared with the corresponding subscale experimental data. Finally, simulations were conducted for full-scale tests and compared with actual in-water data. While the in-water data was limited to propulsor rpm and vehicle velocity, the operating advance ratio could be determined as well as the estimated vehicle thrust. This provided a method to utilize CFD/experiments to bridge the gap between subscale and full-scale tests. The predicted in-water advance ratio of 1.87 was very close to the measured value of 1.75.

INTRODUCTION

Currently, propulsor design is performed through use of various computational fluid dynamics (CFD) codes. A set of potential flow based blade design codes (Propeller Blade Design Code, PBD 14.3) and analysis codes (Propeller Unsteady Force, PUF) were developed at the Massachusetts Institute of Technology, [1-3]. These methods are useful in examining a broader design space as the computational turnaround times are relatively fast. At later stages in the design process, Reynolds Averaged Navier-Stokes (RANS) solvers [4-6] are used for a more detailed examination of the propulsor performance and provide a higher fidelity prediction of in-water performance. As with any CFD based solution, it is necessary to obtain experimental validation data to lend confidence to the validity of the final solutions. For many novel propulsor designs, in-water data generally does not exist to provide this validation. Therefore, once the blades are designed, oftentimes a subscale model is created and tested in a water tunnel to provide needed validation and/or estimates of in-water performance [7-10]. The performance of the subscale propulsor is measured and the results are scaled to estimate the full scale propulsor performance. While full scale in-water testing would be the best indicator of propulsor performance, subscale tests are much more cost effective and allow for more flow and performance data specifically required for CFD model validation to be acquired.

While the above method provides an estimate as to the full scale performance of the new propulsor, this estimate is not always accurate. There are fundamental differences between laboratory testing and in-water testing due to both the Reynolds number of the flow and the change in the flow field associated with the presence of the water tunnel walls. It is widely known [12] that changes in the turbulent boundary layer due to increased Reynolds number can alter both the skin friction (total body drag) as well as influence local flow separation phenomena. For most water tunnel tests, the model can occupy a significant volume in the water tunnel test section resulting in a tunnel blockage effect. This can significantly alter both the drag characteristics of the model body as well as the inflow into the propulsor. Without a proper understanding of both these effects, it is very difficult to utilize CFD and scale model experimental data alone to adequately predict in-water propulsor performance.

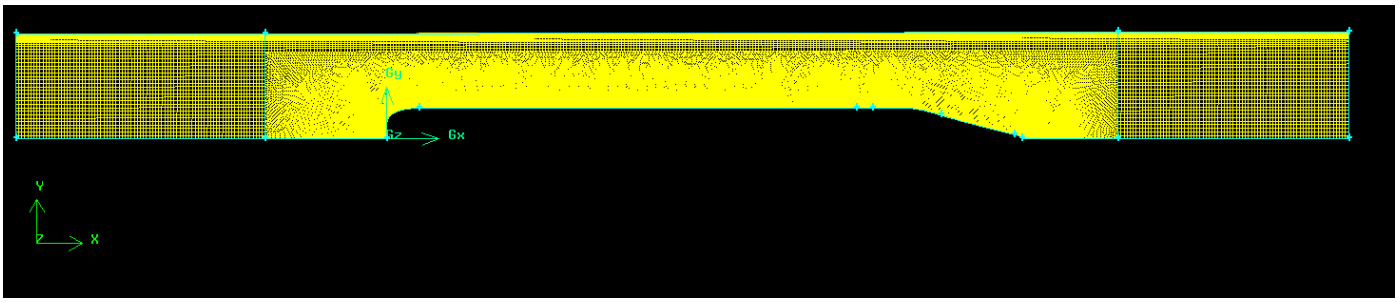

Figure 1: Typical Axisymmetric 2-D Fluent® mesh generated using Gambit® highlighting the water tunnel model mesh.

This paper presents a method to combine CFD modeling with subscale experiments to improve full-scale propulsor performance prediction. With the relatively recent availability of robust commercial CFD software packages and the improvements in high performance computing, it is believed that this is now possible where before this was not the case. This study uses the commercial software package Fluent®, to provide fully viscous, 3-D and axisymmetric RANS solutions to both water tunnel and full scale vehicle propulsor problems. Laboratory experiments were conducted on subscale torpedo models in the 12'' x 12" water tunnel located at the Naval Undersea Warfare Center in Newport, Rhode Island. This model included an operational ducted post-swirl propulsor. Laser Doppler Velocimetry (LDV) was used to measure velocity profiles along the torpedo hull. This experimental data was used to validate the numerical model and determine the Fluent® settings most appropriate to this application. The goal of this study is to utilize CFD solutions to accurately predict the outcome of the subscale water tunnel tests. When this is accomplished, scaling up the geometry and changing the boundary conditions while still maintaining the same Fluent® settings will lend a higher level of confidence to the final in-water solution.

METHODOLOGY:

RANS Solver (Fluent®):

RANS methods were used to compute the 2-D axisymmetric flow as well as a full 3-D formulation to compute the fully coupled rotor/stator/duct problem. The commercial code Fluent® was used as the RANS solver [13]. There is an extensive library of references regarding RANS development and implementation that won't be repeated here. Specific solver settings and grid resolution will be summarized. Bare hull and duct investigations initially utilized a 2-D axisymmetric implicit flow solver with swirl. Figure 1 shows a typical 2-D solution grid. In order to most accurately model the water tunnel configuration, the inlet and outlet are located at their corresponding experimental locations. The grid consists of a mixture of quadrilaterals and triangles. Outflow boundary conditions were prescribed for the exit plane. A realizable k-ε turbulence model with boundary layer resolution on both the body and duct to y+ = 1 was employed. Results from these studies were used to estimate the body and duct drag as well as characterize the effect of the water tunnel. Water tunnel experimental data was used to validate and calibrate the Fluent® solver. A steady 3-D implicit flow solver was used to compute the flow for the rotor, stator, and pedestal geometries (Figure 2). The 3-D solution methodology utilizes a finite volume formulation with a mixture of tetrahedral and brick elements as defined by the grid generator, Gambit®. These computations also employed a realizable k-ε turbulence model with boundary layer resolution on all surfaces to y+ = 1. Second order upwind solutions of the advection term and turbulent kinetic energy were used.

Separate full 3-D RANS solutions using Fluent® were computed for the final rotor and stator blade designs, seen above in Figure 2. For this study the NUWC Light torpedo geometry was used [4]. As this is an existing configuration, there was no need to repeat the design process, and the existing hull, duct, and blade geometries were used. The blade geometries were then integrated into the afterbody and duct solid models to form a single volume, eliminating any gap between the blades and the shroud. For the subscale configuration the water tunnel walls were also incorporated.

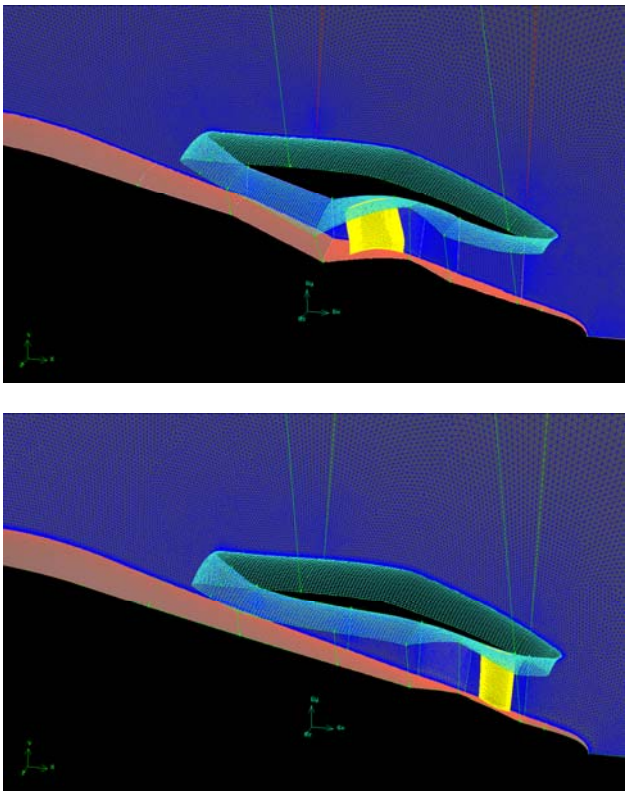

Figure 2: Typical 3-D Fluent® mesh generated using Gambit® highlighting the periodic meshes for the rotor and stator as well as the hull, duct and blade geometries.

A full 3-D solution for every blade in each of the blade rows would be computationally intensive as well as inefficient. Since steady state assumptions were made, a solution using periodic boundary conditions was permitted. This enabled a solution to be obtained from modeling only a single blade. Separate solutions were computed for the rotor and stator geometries since the number of blades in each blade row was different. In order to incorporate the effects of the missing blade row, a momentum source was used to model the blade forces. A volume encompassing the missing blade row was inserted into each model and the momentum sources were assumed constant over that volume. The two solutions were iterated until the blade force residuals were less than 1%. Figure 2 shows the periodic boundaries and the grids for the rotor and stator computational solutions.

Fluent® Solver Settings for 2-Dimensional Analysis

Before analysis could begin, the appropriate Fluent® settings needed to be chosen. There are many options and settings that have been analyzed, not all of which will be enumerated in this paper. A vital component of the computational RANS solver is the turbulence models. Short of performing a direct numerical simulation of the Navier Stokes equations, a very computationally expensive proposition, turbulence models are needed in order to make them tractable for real world applications. According to the literature, the realizable k- ε model would be the best fit for this application. In general, the k- ε model is the standard default in the industry, praised as having "robustness, economy and reasonable accuracy for a wide range of turbulent flows" [13]. The realizable k- ε model was chosen versus the standard model because in comparison it "provides superior performance for flows involving rotation, boundary layers under strong adverse pressure gradients, separation, and recirculation" [13]. This model is a formulation proposed by Shih et al. [12] and includes a different turbulent viscosity formulation and transport equation as compared to the standard k- ε model.

Like with all models there are distinct disadvantages to using the k- ε model as well. It is only valid for fully turbulent flows. It also produces non-physical turbulent viscosities in regions when the domain contains both rotating and stationary fluid zones. While at full scale the flow over the body is assuredly turbulent, at the subscale there could be laminar flow at low velocities. Therefore emphasis was placed on using the experimental data at the higher velocities for validation. The non-physical turbulent viscosity is more of a concern. As will be discussed later, the k- ε model over predicts the turbulent kinetic energy (k). Comparison of the resultant flow fields using many of the available Fluent® solvers confirmed that the realizable k- ε model produced results most consistent with the experimental validation data.

Water Tunnel Experiments

Experiments were conducted in the research water tunnel at the Naval Undersea Warfare Center in Newport, Rhode Island (Figure 3). The tunnel has a 30.48 cm square cross section and a maximum flow speed of 9.1 m/s. The facilities are equipped with closed loop velocity control and have removable plexiglass windows for tunnel access. The NUWC water tunnel slowly expands in the downstream direction to account for boundary layer growth on the walls, minimizing the acceleration of fluid in the 3.05 m long test section. The tunnel has a 3:1 ratio contraction section and a 15.25 cm thick honeycomb mesh with 7.6 mm cells, giving 0.5% maximum turbulence intensity in the center of the tunnel. The tunnel is powered by a 61 cm single stage impeller with a 448 kW electric motor. Two 13.25 kliter water storage tanks, one for fresh water and the other for salt, are used for filling and draining the tunnel. Fresh water is used for all experiments in this work. The water tunnel is equipped with a two component Laser Doppler Velocimetry (LDV) system that was used to acquire velocity data along the model geometry.

The full scale NUWC Light torpedo is 12.75" in diameter and 120" long (32.4 cm x 305 cm). The subscale shroud and propulsor design is summarized by Huyer et-al [4] and was used in these experiments. A 0.3137 scale model of the NUWC Light vehicle was constructed of an Aluminum / SLA / SLS material. The vehicle is 36" long and 4" diameter (91.44 cm, 10.16 cm diameter) and is strut mounted to the water tunnel test section ceiling via a load cell. It incorporates an internally mounted permanent magnet motor, capable of producing 6000 rpm at 2 HP to spin the scale propulsors at freestream velocities of 0 to 20 knots (10.3 m/sec). The propulsor thrust was measured using a load cell. The propulsive efficiency as a function of advance ratio was estimated from the power used by the electric motor. The model consists of 5 modular sections; the nose, the forward body, the mounting section, the motor section, and the tail section. The nose was ballasted to offset the moment incurred by the weight of the motor. The tail includes the propulsor which consists of a shrouded propeller. Figure 4 shows the model in the water tunnel test section. Figure 5 shows the afterbody section with removable rotor and stator sections.

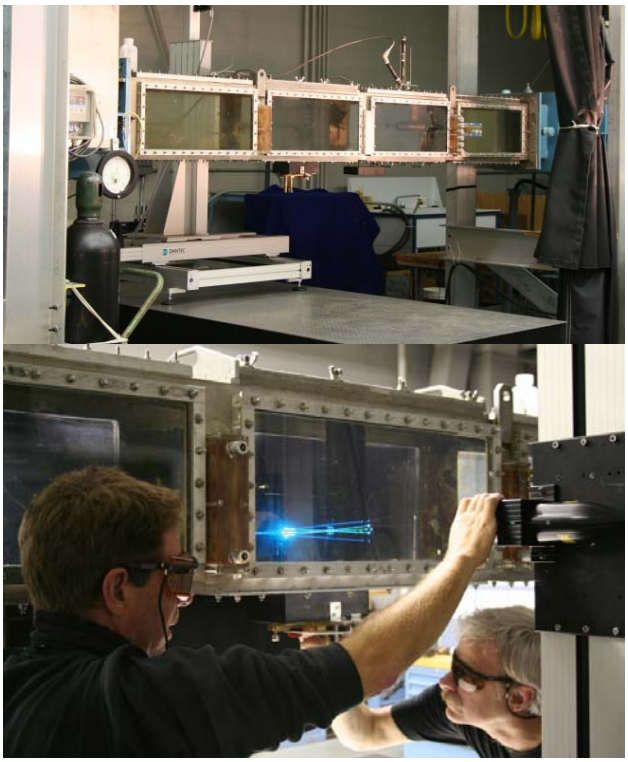

Figure 3: NUWC 12" Water Tunnel

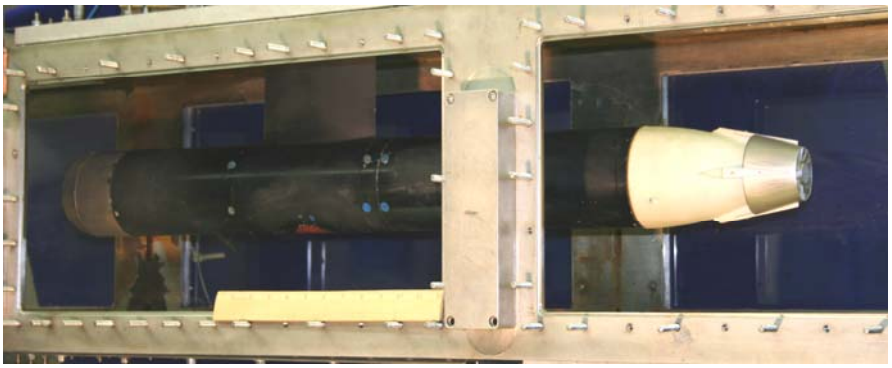

Figure 4: Photograph of the 4" baseline model in the water tunnel test section.

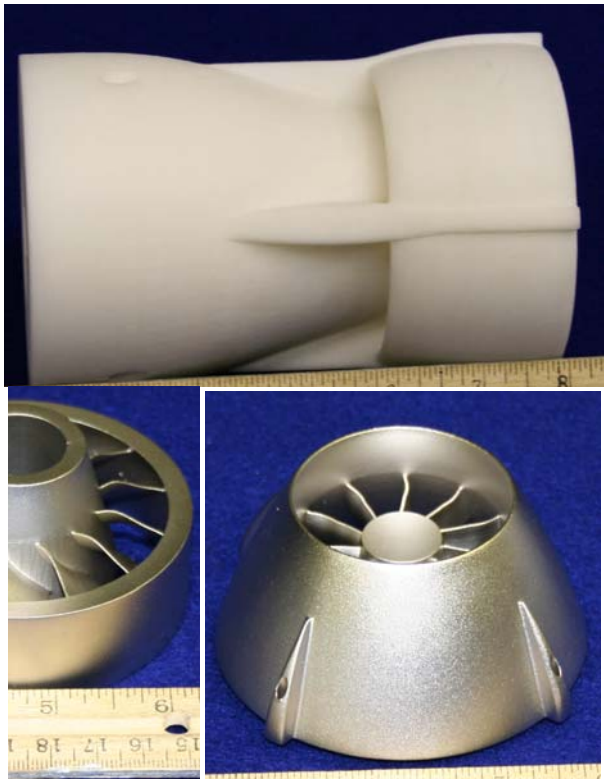

Figure 5: Test model hardware of the afterbody section and rotor and stator blade rows.

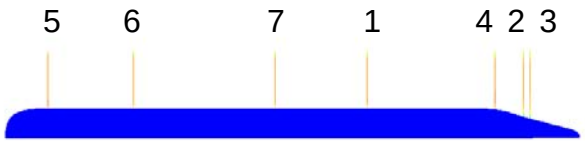

Figure 6: LDV Data Collection Locations

RESULTS:

Model Validation

This study utilized the torpedo geometry of the NUWC Light vehicle as existing LDV measurements were already available to use as validation. The starting point of this study was a two-dimensional Gambit mesh of both the bare body (no shroud/propulsor) and the shrouded bare body. Because these configurations are axisymmetric, they can be modeled using the two-dimensional version of Fluent®, allowing for in-depth analysis of the Fluent® settings at a relatively inexpensive computational cost.

The specific locations of the LDV data for the bare body case are shown in Figure 6 and are designated XL1-7. They were taken at three different speeds; 2, 4, and 8 m/s. These LDV measurements were taken on the underside of the subscale model, 180 degrees away from the strut to minimize the impact of the strut on the flow, as its presence will not be included in the CFD model. The LDV allowed for velocity measurements in two directions with the fluxes in those directions as well, allowing for calculation of the experimental turbulent kinetic energy with Equation 1 (Pope[11]):

$$k = \frac{1}{2}\langle u_i u_i \rangle \tag{1}$$

The flow fields of the numerical and experimental solutions are compared by evaluating the velocity and turbulent kinetic energy profiles. In addition, body drag and advance ratio are used for comparison when the propulsor blades are included in the three-dimensional model.

2-Dimensional initial validation

A two-dimensional model of the subscale vessel inside the water tunnel was created in Gambit to be as consistent with the experimental test set-up as possible. However, due to the nature of a two-dimensional axisymmetric model, certain features of the test setup could not be included. Notably, the rotor, stator, and pedestals are absent from the two-dimensional model. These three features greatly impact the flow field; therefore experimental data of the bare body which did not include these features was used to provide the best comparison for this initial two-dimensional validation study. In order to obtain adequate grid resolution near the walls, boundary layers were put on the hull, shroud, and tunnel walls. The first grid point was set at y+=1, as proscribed by the Fluent® manual [13]. A growth function of 1.2 was used, and 15 layers were included so that the boundary layer along the wall is well resolved. The geometry of this configuration can be seen in Figure 2.

The bare body model was the preliminary test to validate the CFD results. A grid convergence study was performed on the 2-dimensional model with the results shown in Figure 7. The

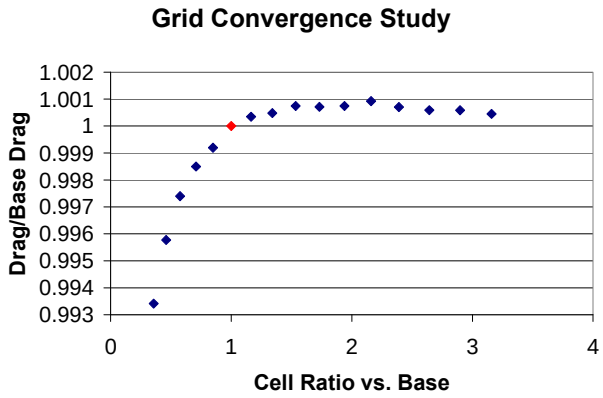

Figure 7: Bare hull drag for a range of grid resolutions.

red dot indicates the base grid that was used, and as can be seen significant increases in grid resolution do not significantly change either the drag values or the velocity profiles over the body. Therefore it can be assumed that the grid resolution used in this study is adequate for comparison to the experimental model.

There is one main difference between the two dimensional model and the water tunnel experimental configuration. Although the hull and shroud geometries are axisymmetric, the tunnel cross section is not. Therefore, in order to approximate the same flow through an axisymmetric tunnel as there is in a square tunnel, the hydraulic diameter of the square tunnel was used as the diameter of the axisymmetric model. This is a valid approximation, the details of which will be explained later.

Figure 8 shows plots of the axial velocity components taken at stations XL-1 and XL-2 corresponding to the mid-body and shroud inlet locations respectively as seen in Figure 6. Boundary layer plots are shown for 2, 4 and 8 m/sec test cases and compare the 2-D Fluent® solutions with the experimental results. As can be seen, at the mid-body locations, there is excellent agreement between the experimental and computational solutions. The experimental data indicate 2% higher velocities in the lower boundary layer region potentially indicating an effective higher Reynolds number. Overall, the agreement is excellent.

The axial profile taken at the XL-2 location was significantly more challenging as this is in the afterbody region. In this region, an adverse pressure gradient forms giving rise to a significant growth in boundary layer thickness. Still, there is excellent agreement between the experimental and computational results. Experimental data continue to show slightly fuller profiles in the afterbody region compared with computational results (2% higher).

Figure 9 shows a plot of the turbulent kinetic energy (TKE) for both experimental and 2-D simulations taken at stations XL-1 and XL-2 for the same test conditions shown in Figure 8. As can be seen, the experimental values illustrate the freestream turbulent velocities with values outside the boundary layer on the order of 0.01. The Fluent® solution does not fully capture this with minimal TKE values. At the mid-body location (XL-1) the CFD solutions predict higher

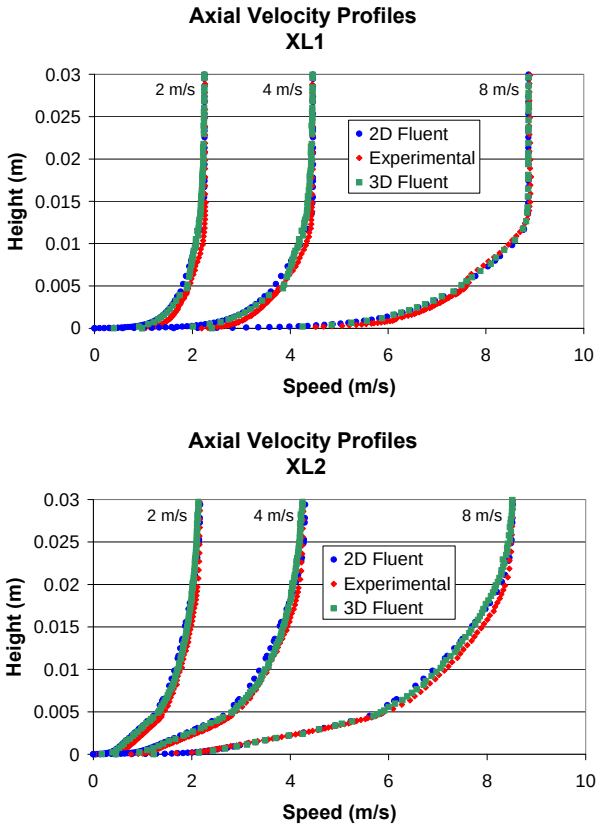

Figure 8: Axial boundary layer velocity profiles taken at the mid-body (XL-1) and afterbody region (XL-3) at freestream velocities of 2, 4 and 8 m/s comparing Fluent® solutions and experimental data.

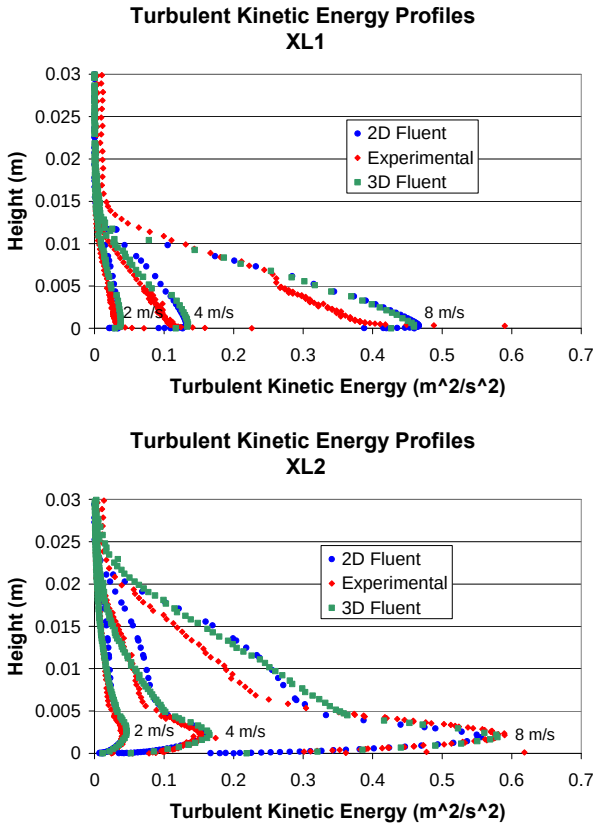

Figure 9: Turbulent kinetic energy (TKE) boundary layer profiles for the same conditions listed in Figure 9.

TKE values in the boundary layer than were seen experimentally. In all cases, TKE values peak at the surface and appear to decrease approximately linearly through the boundary layer. At the afterbody location (XL-2) the behavior is significantly different. Again, the freestream turbulence can be seen in the experimental data. Unlike the mid-body TKE distributions, however, there appears a peak in TKE just above the surface for all three inflow velocity test cases. Fluent® predicts the magnitude and location of this peak very well. As the normal distance is increased, Fluent® slightly over-predicts the TKE similar to the mid-body profiles. Importantly, however, the characteristics of the TKE distributions are equivalent for the CFD simulations and experimental data.

Bare hull drag data were computed and compared with the experimental water tunnel data in Figure 10. Both 2-D and full 3-D Fluent® simulation data are presented. As can be seen, the body drag data agree extremely well with experimental data.

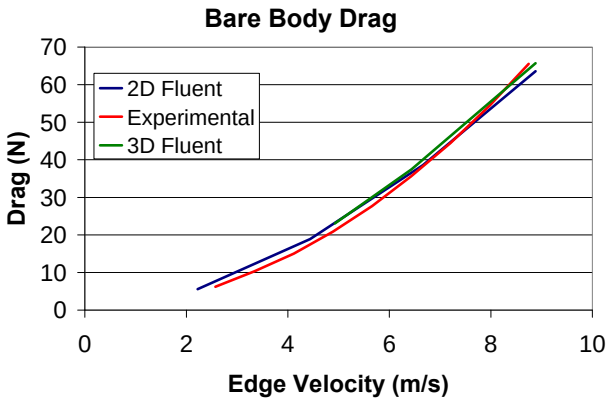

Figure 10: Bare hull drag data in N for the water tunnel velocities examined.

Water Tunnel Effect Characterization

There are two main differences between the subscale configuration and the full scale configuration; the presence of the tunnel walls and the Reynolds number of the flow. The Reynolds number effect has been well documented and can be accounted for. However, the impact of the tunnel walls on the flow presents a greater problem in predicting full scale performance from subscale results. The tunnel blockage effect of the body in the water tunnel chamber is well known to cause accelerated flow over the top of the model due to the constriction in area and the conservation of mass. The axial changes in the edge velocity as a function of the water tunnel size can be seen in Figure 11. It is important to characterize the differences imposed on the flow from the presence of the tunnel walls in order to understand why the advance ratio of the water tunnel configuration is so different from that of the in-water tests.

One immediate answer lies in the definition of the advance ratio (J), seen in Equation 2 where V is the freestream velocity, n is the rotational velocity in Hz, and D is the rotor diameter. For the water tunnel configuration, the V is defined as the inlet velocity upstream of the body, whereas for the open water configuration the V is the edge velocity over the vehicle. This difference must be accounted for when trying to compare the two configurations.

$$J = \frac{V}{nD} \qquad (2)$$

The effect of the accelerated flow on the propulsor due to the tunnel blockage is best visualized by looking at the magnitude of the velocity profiles that go into the rotor, seen in Figure 15 for a variety of water tunnel radii. A range of water tunnel radii were examined that ranged from 4" (10.16 cm) to 24" (60.96 cm) with a freestream case (infinite) included as well. The NUWC water tunnel cas a hydraulic raidus of 6.77" (17.2 cm) The subscale hull radius is 2" (5.08 cm). Figure 11 plots the axial velocities taken at the midpoint between the tunnel centerline and outer wall and illustrates the flow acceleration

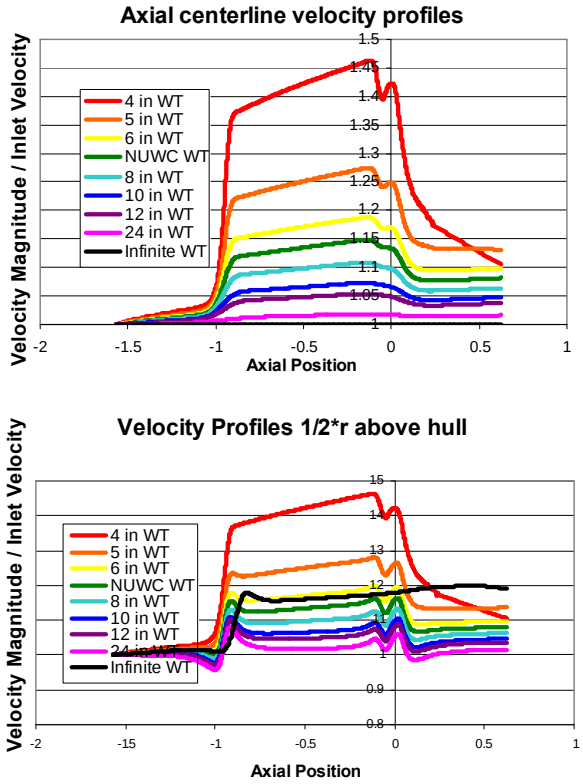

Figure 11: Centerline axial velocity profiles for the range of virtual water tunnels examined scaled by the inlet velocity.

due to the tunnel blockage. For the smallest tunnel (4") peak velocities are approximately 45% greater than the freestream case with peak velocities for the NUWC water tunnel approximately 15% greater than freestream. The velocity increase is non-linear over the body with the velocities decreasing rapidly at the end of the model body. This velocity profile generates a favorable pressure gradient over much of the hull body with an adverse pressure gradient generated in the afterbody region.

Plots of the axial velocity contours are shown in Figure 12 for virtual water tunnels with radii of 4", 10" and infinite with comparison with the NUWC water tunnel. It is clear that as the water tunnel radius is increased, the relative flow

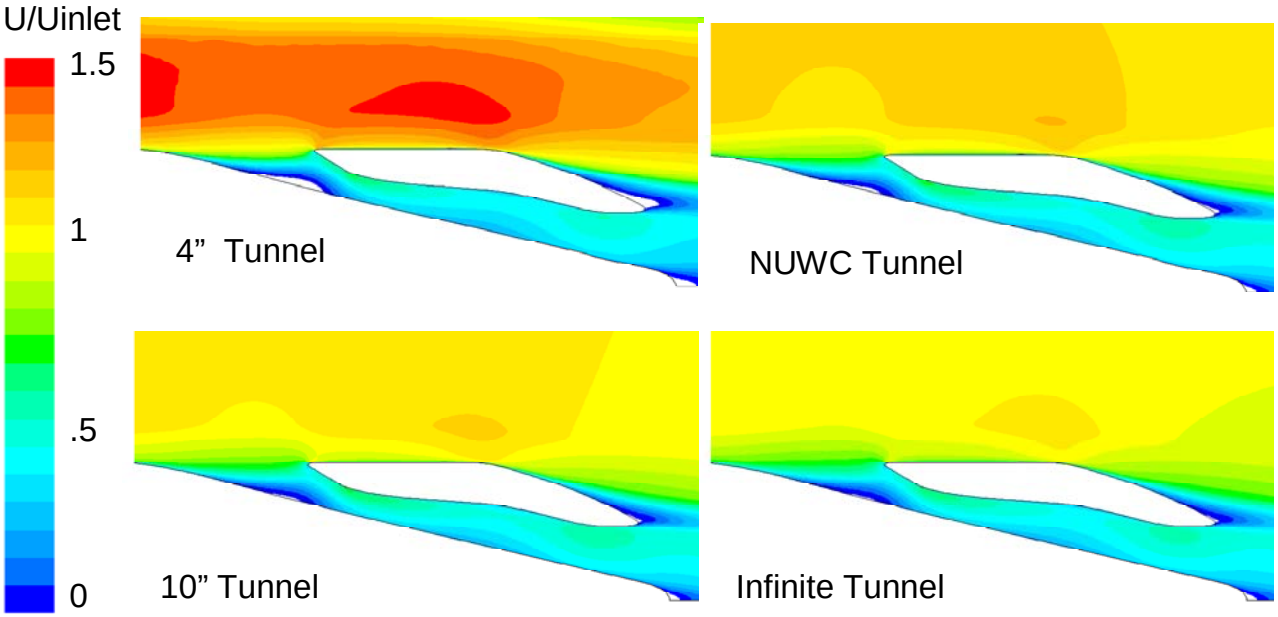

Figure 12: Axial velocity contour plots of the flow in the vicinity of the duct.

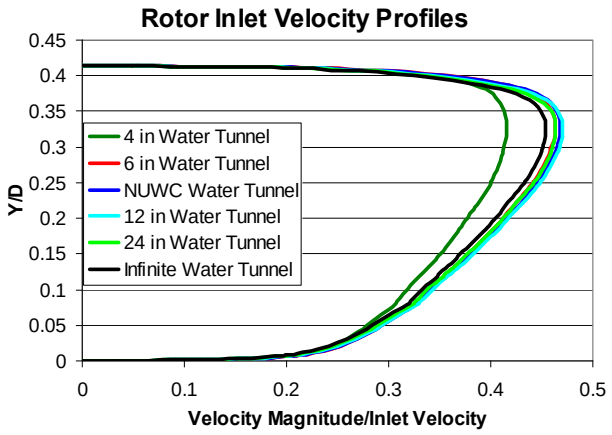

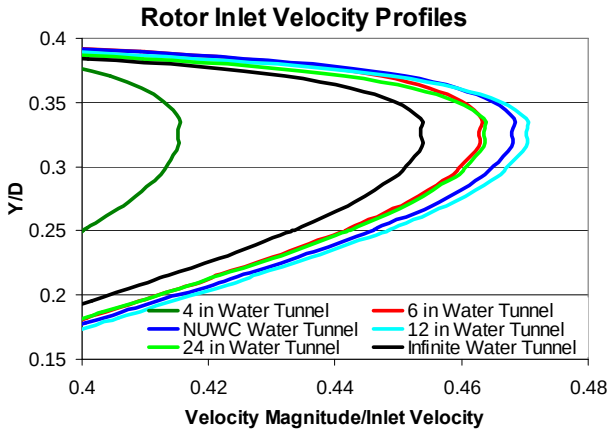

Figure 13: Rotor inlet velocity magnitude profiles with data scaled by the inlet velocity for the range of tunnel radii examined.

velocities in the afterbody region are decreased as highlighted in Figure 11. The effect of the adverse pressure gradient can be illustrated in these plots. Notice that for the 4" tunnel, there is a large separation bubble in the vicinity of the duct leading edge and contains a reverse flow region. This separation bubble is smaller for the NUWC water tunnel and 10" water tunnel. For the infinite tunnel, there is even less separation, permitting more flow through the duct.

Velocity profiles taken at the rotor leading edge are plotted in Figure 13 for the range of tunnel radii examined. The data presented in this figure are scaled by the inlet velocity. It is interesting to note that the data do not scale with the edge velocity, as was seen with the surface pressure data. At first glance, the velocity profiles appear very similar, except for the 4" water tunnel case. The scale is blown up for the plot on the right, revealing an unexpected trend. Initially, as the water tunnel radii are increased, peak rotor inflow velocities are increased, but only up to the 12" water tunnel radius. The peak velocities actually decrease as the water tunnel radius is increased to 24" followed by the infinite water tunnel. This phenomenon suggests that while the body drag increases with reduced tunnel radius, there is little overall change in the rotor inflow velocity profile. This is an important result as this affects both propulsor performance as well as the measured self-propulsion point.

Figure 14 plots the hull surface pressure coefficient distributions with pressures scaled by both the inlet velocity as well as the edge velocity (defined as the velocity at the model mid-body equidistant from the tunnel wall and model surface). The effect of the tunnel blockage can clearly be seen for the data are scaled by the inlet velocity with lower pressures over the body surface. When scaled by the edge velocities, the 4" data still remains separate, but the 6" tunnel and NUWC tunnel data appears to collapse in the mid-body region as well as the 12" and infinite tunnel cases.

Figure 15 plots the surface pressure coefficient distributions for the afterbody and shroud scaled by the edge velocity. As can be seen in the afterbody region, when scaled by the edge velocity, the data appear to collapse. There still seems to be a difference between the 6" and NUWC water tunnel data and the 12" and infinite case data. The shroud surface pressure

Table 1: Computed edge Velocity and Drag Values for Tunnel Radii Examined

WT Radius	Edge Velocity (m/sec)	Drag (N)	Cd (Inlet)	Cd (Edge)	Drag Ratio
4.00	10.25	200.97	0.7760	0.4729	3.47
5.00	10.04	132.76	0.5127	0.3253	2.29
6.00	9.09	106.46	0.4111	0.3183	1.84
NUWC WT	9.10	95.52	0.3688	0.2849	1.65
8.00	8.67	85.27	0.3293	0.2801	1.47
10.00	8.47	76.44	0.2952	0.2634	1.32
12.00	8.35	71.74	0.2770	0.2542	1.24
24.00	8.12	63.17	0.2439	0.2366	1.09
Infinite	8.00	57.91	0.2236	0.2236	1.00

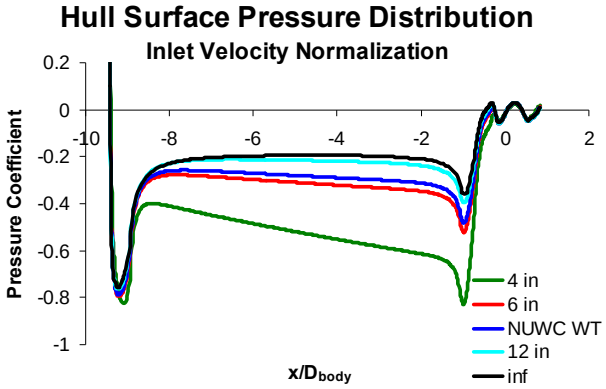

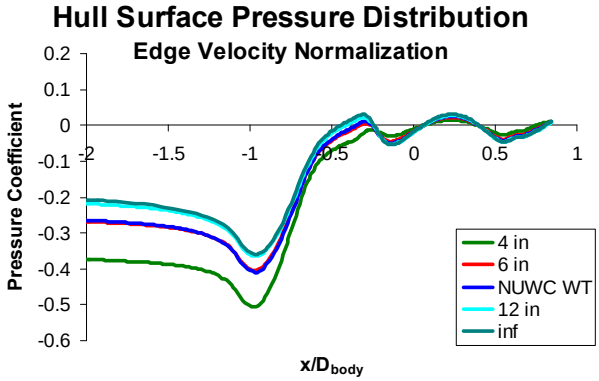

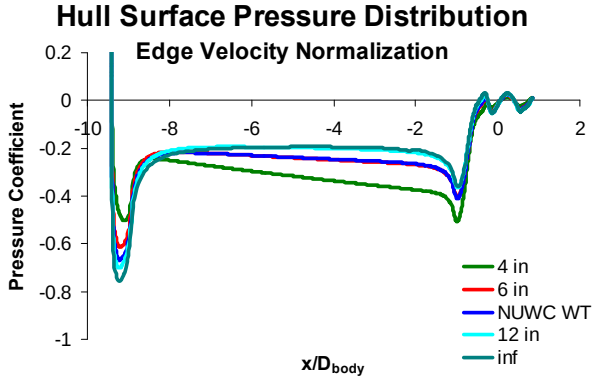

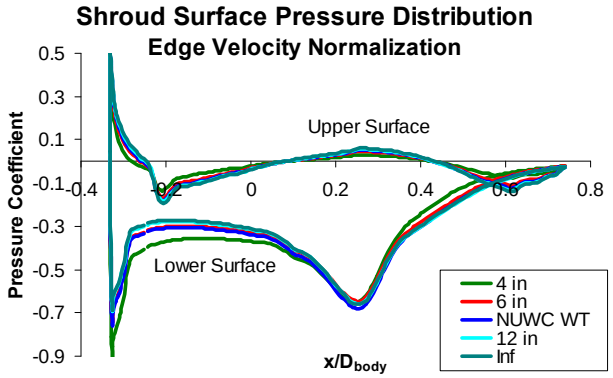

Figure 14: Hull surface pressure coefficient distributions with pressure data scaled by the inlet velocity and edge velocity for the range of tunnel radii examined.

Figure 15: Hull afterbody and shroud surface pressure coefficient distributions with pressure data scaled by the edge velocity for the range of tunnel radii examined.

data appear to collapse for all water tunnel radii examined, with the exception of the 4" tunnel case.

Edge velocity and drag data are listed in Table 1. Drag coefficients were scaled both by inlet as well as edge velocity with the drag ratio indicating the relative increase in drag based on the infinite water tunnel case. It is immediately clear that the drag values do not collapse when scaled by the edge velocity, indicating more complex physics are involved. The data show that the base drag data are increased by 65% for the NUWC water tunnel.

Three Dimensional Bladed Propulsor Model

When initially moving to three dimensions, the study of the bare body configuration was continued in order to be able to directly compare the two dimensional solutions to the three dimensional solutions. One complication of this modeling was that the water tunnel itself is square. Because the cross section is not axisymmetric, at the minimum a 90 degree quarter of the tunnel must be modeled in order to accurately represent the square cross section. There is an upper limit on the computational power of the resources available for use in this study; therefore meshes need to be kept under a certain size. The quarter model, by virtue of being ¼ the size of the full tunnel, therefore allowed for much higher grid resolution in comparison. Symmetry boundary conditions were imposed on the interior sides of the quarter wedge.

Velocity planes were extracted at the seven locations seen in Figure 6 and circumferentially averaged to compare with the experimental data and the two-dimensional solution. The grid

resolution of the three dimensional model is significantly coarser than the two-dimensional model; however the results match both the 2-D data and the experimental data well as seen in Figures 9 and 10.

Once the 3-dimensional bare body model was validated, the shroud, pedestals, and propulsor needed to be incorporated. This presented a problem in that there are an different number of rotors, stators, and pedestals, therefore the entire cross section would need to be modeled rather than just a quarter. Computationally this was too expensive to accomplish with adequate grid resolution; an alternative needed to be implemented. A study was conducted in order to determine whether a circular water tunnel with the same hydraulic diameter as the square water tunnel would produce similar results as compared to the quarter model close to the hull. Because the area of interest here is on the body of the torpedo, rather than at the wall of the tunnel, it was believed that the error from the substitution of an axisymmetric cross section would be negligible. This hypothesis was corroborated by CFD studies of both the square and circular cross sections, seen below in Table 2, resulting in discrepancies in the body drag on the order of 5%. The possibility of an axisymmetric circular wedge model allows for increased resolution over the square water tunnel as a smaller percentage of the total flow needs to be modeled. The sides of the wedge (blue in below right) are modeled as having periodic boundary conditions in order to impose symmetry of flow over both sides.

Unlike with in-water runs, for both the water tunnel configuration and the numerical configuration it is possible to run the propeller at speeds other than the self propulsion speed. Therefore the self propulsion point is defined as the point where the thrust produced by the propulsor equals the drag produced by the body, resulting in zero net axial force. To accurately determine the point of self-propulsion of the model, it is important to take into account all aspects of the geometry that would significantly influence body drag. Each of the important features, the rotor row, stator row, and the pedestals, has a different circumferential number of components, therefore a different size wedge must be made for each. It is important to note that not all features of the geometry have been modeled and the pedestals in particular have been smoothed in order to ensure that the CFD code would mesh the geometry. The pedestal mesh can be seen in Figure 16 below and the rotor and stator meshes are depicted in Figure 2.

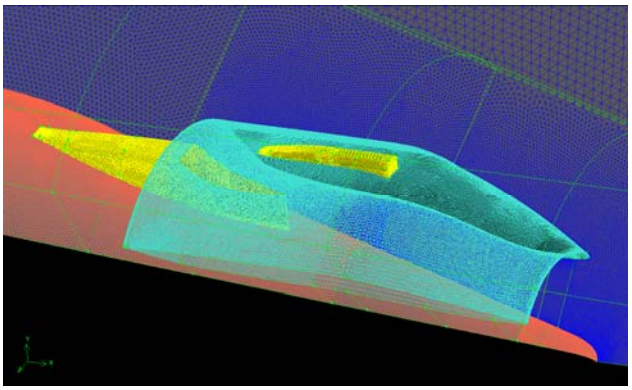

Figure 16: Mesh of pedestal geometry

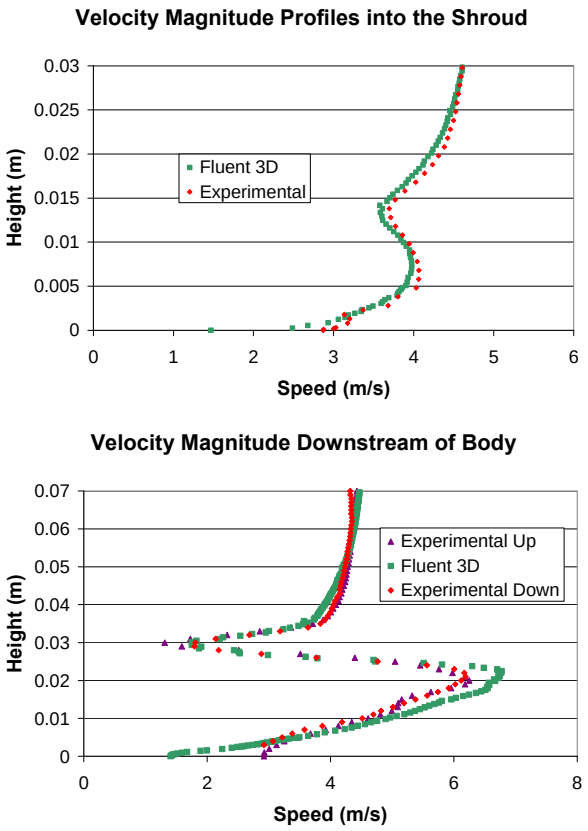

Figure 17: Velocity profile comparison for NUWC-light geometry with propulsor spinning

By modeling each component separately, the effect of interactions between the features is lost. A pseudo-coupled rotor-stator solution is produced by using momentum sources to simulate the effect of the other blade row while iterating between the two models until the force terms converge within 1%. Unfortunately the same cannot be done with the pedestals. Due to the complex geometry associated with the pedestals, it was impossible to attach a boundary layer to the walls of the model, like has been done with the rotor and stator models. To accurately determine the effect of these pedestals, another model with the same element density, the same lack of boundary layers, and without the pedestal geometry needed to be constructed for comparison. The effect of the pedestals on the drag can be approximated from the increase in drag on this coarse mesh. This percentage increase in drag can then be used to approximate the effect the pedestals would have on an sufficiently resolved mesh. The results of this study were that the inclusion of the pedestals increased the vehicle drag by 6% in the subscale model. In the full-scale model the vehicle drag was increased by 18%.

The results of these three models are then combined to produce the most complete approximation of the flow around the body short of modeling both the entire cross-section and every topographical feature. Like with the bare body case, while the numerical velocity profiles are in very good agreement with the experimental velocity profiles, the numerical turbulent kinetic energy profiles are consistently higher in magnitude than the experimental profiles as seen in Figure 17. The top plot shows the velocity magnitude profile immediately upstream of the shroud with the rotor spinning.

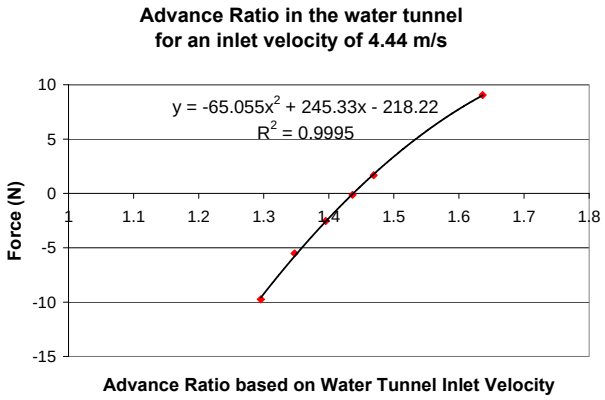

Figure 18: Profile of the force produced by the subscale water tunnel numerical model at varying advance ratios

Table 3: Sample drag distribution over the model components

Advance Ratio = 1.436	
Component	**Total Axial Force (N)**
Hull	49.283
Rotor Blades	-34.231
Shroud	-12.882
Stator Blades	-3.659
Pedestals	1.362
Total	**-0.127**

Table 4: Comparison of numerical and experimental advance ratio calculation

Configuration	Advance Ratio % difference
Subscale	10.80%
Full Scale	6.81%

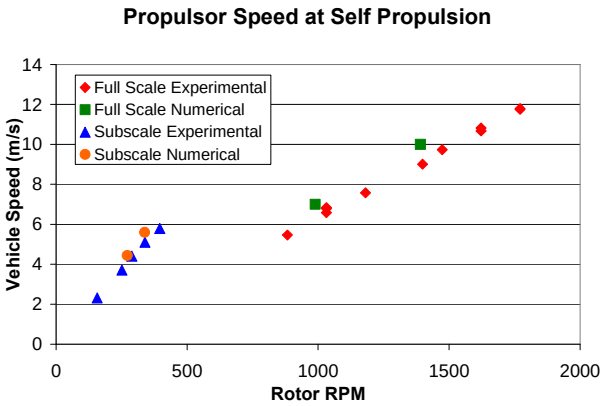

Figure 19: Comparison of Numerical and Experimental propulsor speeds at self propulsion

The shroud is at a height of about .014 m, and the spinning rotor pulls the flow into the duct, causing the jet on the lower half of the profile. The bottom plot on Figure 17 shows the velocity magnitude profile downstream of the torpedo body. For this location, LDV measurements were taken both above the centerline and below, which is why there are two experimental profiles with which to compare the numerical profile. However the ultimate figure of merit is determining the advance ratio of the numerical self propulsion point and comparing it to that found in the water tunnel. This is done through iteration at different rotor RPM. Figure 18 shows the results of six different advance ratios and the resultant forces for the subscale configuration at an inlet velocity of 4.44 m/s. The point of self propulsion is the intersection of the trend line and y=0. Numerically, this occurs at an advance ratio of 1.437. A breakdown of the component forces is shown in Table 3.

When determining the point of self-propulsion, the axial forces from all three models are combined. As can be seen in Table 3, the hull, shroud, and rotor blade forces are taken from one model. The stator blades forces are taken from another model and the pedestal forces are estimated using the percentage bare body drag increase obtained from the very coarse pedestal mesh discussed earlier. When the thrust produced by the propulsor at a given rotational speed exactly cancels out the drag of the body, self propulsion is reached. The problem with this method lies in the fact that there are additional sources of drag that are not included in any of the models.

Because not all drag sources are being modeled, the numerically calculated advance ratio will be higher than the experimentally calculated advance ratio as the propulsor needs to spin slower to overcome this lower drag, seen in Table 4. For the purpose of this study, the advance ratio in relation to the water tunnel configuration is calculated using the inlet velocity, which for an open water case would be the freestream velocity. However, because this value does not also correspond to the edge velocity, the full scale and the sub scale advance ratios are not comparable. This is one of the main advantages to using CFD to model both configurations. Without changing the settings or the underlying physics, one can obtain numerical predictions for both configurations.

Once the subscale model is completed, the full-scale geometry is modeled. Unlike with the subscale version, the only available data with which to compare to the numerical model is the advance ratio. In terms of geometry, the body geometry is proportional to the subscale; however the boundary conditions extend to infinity, rather than being bounded at the water tunnel walls.

The results of the full scale analysis were very similar to the sub scale analysis. Like with the subscale, it was expected that the numerically determined advance ratio would be higher than the experimentally found value due to the inability to incorporate all drag sources into the model, including the fins. Indeed, the numerically found advance ratio for the full scale configuration was about 7% higher than the experimental value. Figure 19 shows a comparison of the numerical and experimental propulsor speed at self propulsion for the subscale and full scale vehicles

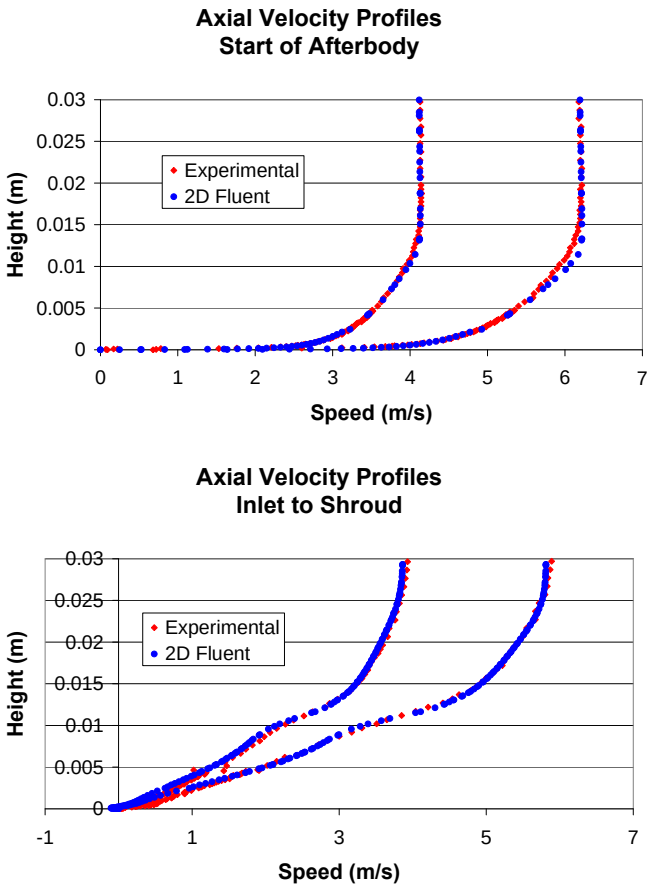

Figure 20: Velocity profile comparisons for Baseline Geometry

Model as a Predictive Tool

Initially, experimental data was only available for the NUWC Light geometry. This data was used to validate the model and determine which settings for the CFD software produced the best solution. However, the ultimate goal of this project was to create a process whereby the Fluent® code could predict the outcome of the experimental subscale runs without having to use such extensive experimental data to validate the model. To this end, additional LDV profiles were taken for another afterbody geometry, referred to as the baseline geometry. The baseline geometry was run with the same settings as the NUWC Light geometry and the numerical results were compared to the experimental data, as seen in Figure 20. Due to time constraints this predictive study was limited to two-dimensional shrouded bare body; however the numerical and experimental velocity profiles are in very good agreement with each other, lending confidence to the hypothesis that this method can be used to determine in-water performance characteristics for any torpedo model with the same basic shape.

CONCLUSION

A combined experimental/numerical methodology to better predict in-water propulsor performance has been presented. The method utilizes both sub-scale water tunnel experimental data coupled with computational fluid dynamics to predict and extend the data to full-scale. 2-D simulations were shown to be in excellent agreement with water tunnel velocity and hull drag data. (See Figures 8-10). This method relied on providing an understanding of the influence of the water tunnel on the flow physics. In this way full 3-D numerical predictions could be tailored to better predict the propulsor performance.

Specifically, examination of the water tunnel demonstrated some non intuitive effects. The virtual study showed that as the effective water tunnel radius was decreased, body drag data was increased significantly. These drag increases did not scale with the edge velocity, however. Surface pressure data did scale better with the edge velocity, but there were still significant differences. Finally, rotor inflow velocity did not appear to vary significantly with the water tunnel radius.

When specifically looking at the NUWC water tunnel as compared to the infinite water tunnel, results arise which account for the discrepancy in advance ratio from the full scale to the sub scale. The accelerated flow from the walls of the water tunnel cause the body drag to almost double as compared to a case where the boundary goes to infinity. This means that that so-called self-propulsion point in the tunnel is not the self-propulsion point for the vehicle in the open water due to the fact that in order to reach this point, the propulsor must spin much faster in order to overcome the additional drag. Additionally, there is a slightly different inflow into the propulsor, resulting in different propulsor characteristics. The propulsor design process utilizes the inflow velocity profile into the rotor to optimally shape the blades. Any changes in this profile will result in differences in the performance of the propulsor.

The ultimate goal of this study was to develop a method whereby CFD can be used in order to predict full-scale in-water propulsor performance. However, like all numerical models, there needs to be model validation through use of experimental data. Because full scale data is extremely difficult and expensive to acquire, subscale testing is performed. This study has shown that the commercially available CFD code, Fluent®, is capable of reproducing and predicting the flow field around the subscale body. Additionally it can be used to predict the full scale advance ratio of the propulsor, which is the ultimate figure of merit. However, there is some discrepancy between the numerically predicted advance ratio and the experimentally observed advance ratio, both for the subscale and full scale configurations. One explanation is that the combination of the three models discussed earlier, the rotor, stator, and pedestal models; still do not account for all of the drag on the body because they do not encompass the entire geometry. Therefore in determining the point of self propulsion, the numerically predicted advance ratio will be higher than the experimentally determined value. However, even with this slight discrepancy, the numerical model allows the researcher to take two separate configurations, with different physics behind the flow fields due to the different boundary conditions, and produce a reasonable estimate of the propulsor performance for both configurations. Indeed, the approximation produced from the numerical model is much closer to the experimental full scale value than the value that was estimated from the experimental subscale testing. Provided that most torpedo configurations have the same basic body shape, it is probable that no matter the propulsor

geometry, the excess drag produced by the body that is not modeled by the CFD will remain relatively constant, therefore the calculated numerical advance ratio will overestimate the actual full scale in-water advance ratio by a consistent percentage.

ACKNOWLEDGEMENTS:
This research was sponsored by the Naval Undersea Warfare Center Division Newport under the New Professional Research Program and the Office of Naval Research under Contract N0001410WX20326, Dr. Scott Hassan program manager.

REFERENCES:

[1] Kerwin, J.E., Lee, C.S., "Prediction of Steady and Unsteady Marine Propeller Performance by Numerical Lifting Surface Theory," *Transactions of the Society of Naval Architects and Marine Engineers*, 86, 1978.

[2] Kerwin, J.E., "Marine Propellers," *Annual Review of Fluid Mechanics,* 18 (1986) 367-403.

[3] Hahn, N.J., Renick, D.H., Taylor, T.E., "PUF-14.4: An Unsteady Analysis Code for Wake-Adapted, Multi-stage Ducted Propulsors," Massachusetts Institute of Technology Department of Ocean Engineering, December, 2000.

[4] Huyer, S.A., Fennel, W., Geurtsen, L., Jandron, M., Oliver, S., "Design and Fabrication of the NUWC Light Propulsor," Proceedings from the Undersea Defence Technology Conference, Europe, Glasgow, Scotland, UK, June 2008.

[5] Lee, Y.T., Hah, C., Loellbach, J., „Flow Analyses in a Single-Stage Propulsion Pump," *J. Fluids Engr*., Vol. 118, pp. 240-248, April 1996.

[6] Carlton, J. Marine Propellers and Propulsion, Second Edition, Elsevier Publishing, 2007.

[7] McCormick, B.W., Eisenhuth, J.J., "Design and Performance of Propellers and Pumpjets for Underwater Propulsion," *AIAA Journal*, Vol. 1, No. 10, pp. 2348-2354, 1963.

[8] Dang, D.Q., Norrie, D.H., "The Unsteady Pressure Field of a Ducted Impeller," *J. Fluid Mech*., Vol. 90, part 2, pp. 209-226, 1979.

[9] Zierke, W.C., Straka, W.A., Taylor, P.D., "An Experimental Investigation of the Flow Through an Axial-Flow Pump," *J. Fluids Engr*., Vol. 117, pp. 485-409, Sept. 1995.

[10] Hughes, M.J., Kinnas, S.A., Kerwin, J.E., "Experimental Validation of a Ducted Propeller Analysis Method," *J. Fluids Engr*., Vol. 114, pp. 214-219, June 1992.

[11] Pope, Stephen Turbulent Flows, Cambridge University Press, New York, 2000.

[12] T.-H. Shih, W. W. Liou, A. Shabbir, Z. Yang, and J. Zhu. A new k-e Eddy-Viscosity Model for High Reynolds Number Turbulent Flows – Model Development and Validation. *Computers Fluids,* 24(3):227-238

[13] Various Authors, Fluent® Users Guide, Fluent.Inc.